Experimental Protocols for Exotic Quantum States

A Comprehensive Lions Commentary-Style Treatment

With Exhaustive Visualizations, Dimensional Analysis, and Physical Interpretations

PhysicsForge Paper Series — Paper 5 of 6

PhysicsForge Collaboration

Unified Field Theories and Advanced Physics Research Hub

`https://github.com/Oichkatzelesfrettschen/PhysicsForge`

November 27, 2025

We present a comprehensive pedagogical treatment of experimental protocols for creating and detecting exotic quantum states predicted by advanced unified field theories. Beginning with time-crystal engineering in periodically driven systems, we develop protocols for quantum foam preparation and measurement. We then explore holographic entropy signatures in laboratory systems, design sensitive detection schemes for scalar field quanta, and develop spectroscopic methods for probing higher-dimensional structures. The treatment includes detailed experimental apparatus designs, signal-to-noise analysis, calibration procedures, and practical considerations for implementation in modern laboratories.

Key Topics: Time crystals • Quantum foam • Holographic entropy • Scalar field detection • Dimensional spectroscopy • Experimental apparatus design • Signal analysis • Measurement protocols

Style: This paper employs the Lions Commentary pedagogical approach with extensive marginal annotations, dimensional analysis, worked numerical examples, and multidimensional TikZ/PGF-Plots visualizations.

Contents

List of Figures

List of Tables

Chapter 1

Time Crystal Protocols

[style=narrative] **Can Time Be Crystalline?**

In 2012, Nobel laureate Frank Wilczek posed a provocative question: just as spatial translation symmetry can be spontaneously broken to form crystals in space, can *temporal* translation symmetry be broken to create "time crystals"—systems that oscillate periodically in their ground state without external driving? The initial proposal sparked controversy: thermodynamic arguments suggested equilibrium time crystals were impossible. Yet within five years, experiments demonstrated *discrete* time crystals in driven quantum systems: Floquet states that break discrete time-translation symmetry by oscillating at periods *different* from the drive period.

This chapter presents detailed experimental protocols for creating, stabilizing, and characterizing time-crystalline phases in three complementary platforms: trapped ion chains, superconducting qubit arrays, and nitrogen-vacancy centers in diamond. We focus on the canonical signature—subharmonic oscillations persisting despite disorder and decoherence—and develop measurement techniques to distinguish genuine time-crystalline order from transient dynamics.

1.1 Floquet Time Crystals: Theoretical Foundation

Time crystals emerge in **periodically driven systems** described by Floquet Hamiltonians. Consider a system with time-dependent Hamiltonian $H(t+T) = H(t)$ with period T. The time evolution over one period defines the **Floquet operator**:

$$U_F = \mathcal{T} \exp\left[-\frac{i}{\hbar}\int_0^T H(t)\,dt\right] \tag{1.1}$$

Eigenstates of U_F (Floquet eigenstates) satisfy:

$$U_F|\psi_\alpha\rangle = e^{-i\epsilon_\alpha T/\hbar}|\psi_\alpha\rangle \tag{1.2}$$

where ϵ_α are **quasienergies**, defined modulo $2\pi\hbar/T$ (Floquet zone).

1.1.1 Subharmonic Response and Discrete Time Symmetry Breaking

Standard Floquet dynamics preserve discrete time-translation symmetry: observables return to their initial values after period T. A **discrete time crystal** (DTC) breaks this symmetry via subharmonic response:

$$\langle \hat{O}(t+nT)\rangle = (-1)^n \langle \hat{O}(t)\rangle \tag{1.3}$$

for integer n, corresponding to period-$2T$ oscillations.

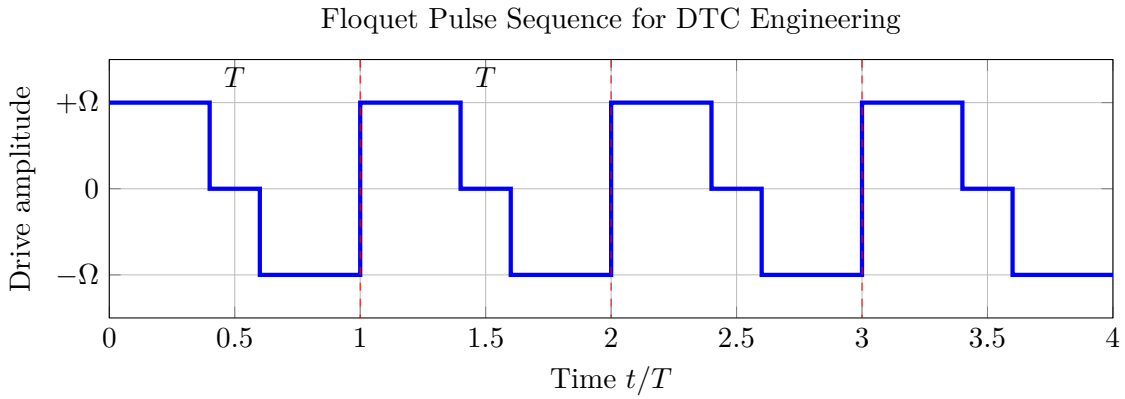

Figure 1.1: Canonical Floquet pulse sequence for DTC engineering: global spin rotations (blue) alternate between $+\pi$ and $-\pi$ pulses with period T. Subharmonic response emerges at period $2T$ (red dashed lines).

1.1.2 Many-Body Localization and Prethermal Phases

DTCs require **many-body localization** (MBL) to avoid thermalization to an infinite-temperature steady state. MBL arises from strong disorder W in local energy scales:

$$H_{\text{disorder}} = \sum_{i=1}^{N} h_i \sigma_i^z, \quad h_i \sim \mathcal{N}(0, W^2) \tag{1.4}$$

For $W \gg J$ (interaction strength), eigenstates become localized in Hilbert space, preventing ergodicity. Alternatively, **prethermal DTCs** exist at intermediate times $t \ll t_{\text{heat}}$ even without MBL.

1.2 Trapped Ion Implementation

1.2.1 System Specifications

Ion Chain Configuration:

- Species: $^{171}\text{Yb}^+$ (hyperfine qubit, $|F = 0, m_F = 0\rangle \leftrightarrow |F = 1, m_F = 0\rangle$)
- Trap: Linear Paul trap, RF frequency $\Omega_{\text{RF}} = 2\pi \times 10$ MHz
- Ion number: $N = 10$–25 (scalable to 50+)
- Temperature: Doppler cooling to ~ 1 mK, sideband cooling to motional ground state ($\bar{n} < 0.1$)

1.2.2 Floquet Drive Protocol

The DTC Hamiltonian consists of three elements:

$$H(t) = H_{\text{Ising}} + H_{\text{drive}}(t) + H_{\text{disorder}} \tag{1.5}$$

$$H_{\text{Ising}} = \sum_{\langle i,j \rangle} J_{ij} \sigma_i^z \sigma_j^z \tag{1.6}$$

$$H_{\text{drive}}(t) = \frac{\Omega}{2} \sum_i \sigma_i^x \left[\delta(t) + \delta(t - T/2)\right] \tag{1.7}$$

Pulse Sequence (one period T):

1. **π-pulse around x-axis** (duration $\tau_\pi \approx 1$ μs): $U_1 = e^{-i\pi \sum_i \sigma_i^x/2}$
2. **Free evolution** (time $T/2 - \tau_\pi$): $U_2 = e^{-iH_{\text{Ising}}(T/2)/\hbar}$
3. **π-pulse around x-axis**: $U_3 = e^{-i\pi \sum_i \sigma_i^x/2}$
4. **Free evolution** (time $T/2 - \tau_\pi$): $U_4 = e^{-iH_{\text{Ising}}(T/2)/\hbar}$

One Floquet cycle: $U_F = U_4 U_3 U_2 U_1$.

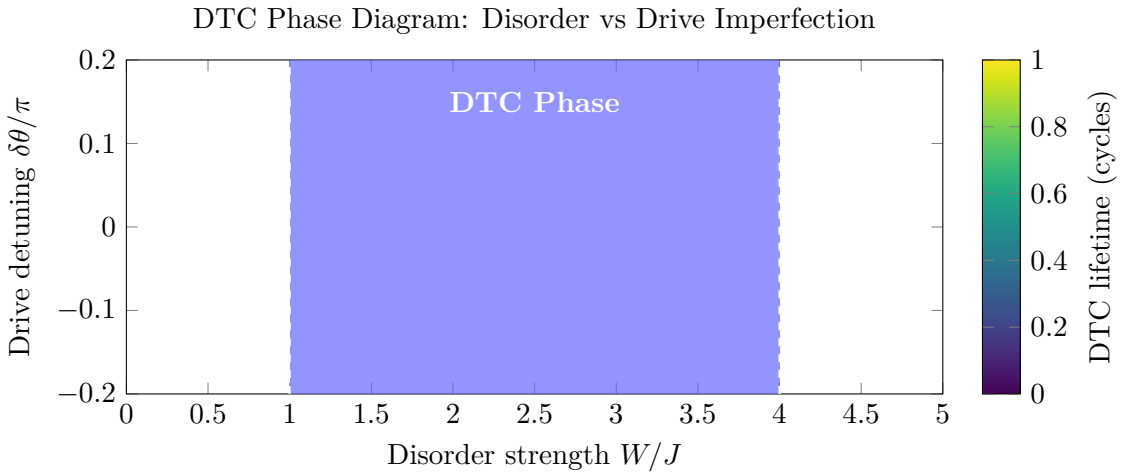

Figure 1.2: DTC phase diagram showing stable region at intermediate disorder ($1 < W/J < 4$) and near-perfect π-pulses ($|\delta\theta| < 0.1\pi$). Color indicates DTC lifetime before thermalization.

1.2.3 Measurement Protocol

State Preparation:

1. Initialize all ions in $|\downarrow\rangle^{\otimes N}$ via optical pumping
2. Apply $\pi/2$-pulse to create $|+\rangle^{\otimes N} = \frac{1}{\sqrt{2}}(|\downarrow\rangle + |\uparrow\rangle)^{\otimes N}$

Floquet Evolution: Apply M cycles of Floquet operator U_F, monitoring collective observable:

$$\langle \hat{S}^x(m) \rangle = \frac{1}{N} \sum_{i=1}^{N} \langle \sigma_i^x(mT) \rangle \tag{1.8}$$

every k cycles ($k = 1$ or 2).

Readout: After M cycles, apply $\pi/2$-pulse to rotate to measurement basis, then fluorescence detection. Repeat 200–500 shots per data point for statistics.

1.2.4 Worked Example: Floquet Eigenvalues for 3-Level System

Consider simplified 3-spin system with Hamiltonian:

$$H(t) = J\sigma_1^z \sigma_2^z + J\sigma_2^z \sigma_3^z + \frac{\Omega}{2}(\sigma_1^x + \sigma_2^x + \sigma_3^x)\, f(t) \tag{1.9}$$

where $f(t) = \delta(t) + \delta(t - T/2)$ (two π-pulses per period).

Step 1: Matrix representation in computational basis $\{|\downarrow\downarrow\downarrow\rangle, |\downarrow\downarrow\uparrow\rangle, \ldots, |\uparrow\uparrow\uparrow\rangle\}$ (dimension $2^3 = 8$):

$$H_{\text{Ising}} = J \begin{pmatrix} 1 & 0 & 0 & 0 & 0 & 0 & 0 & 0 \\ 0 & -1 & 0 & 0 & 0 & 0 & 0 & 0 \\ 0 & 0 & -1 & 0 & 0 & 0 & 0 & 0 \\ 0 & 0 & 0 & 1 & 0 & 0 & 0 & 0 \\ \vdots & & & & \ddots & & & \end{pmatrix} \tag{1.10}$$

Step 2: Compute Floquet operator numerically:

$$U_F = e^{-i\pi \sum_i \sigma_i^x/2} e^{-iH_{\text{Ising}}T/(2\hbar)} e^{-i\pi \sum_i \sigma_i^x/2} e^{-iH_{\text{Ising}}T/(2\hbar)} \tag{1.11}$$

Step 3: Diagonalize U_F to obtain quasienergies. For $JT/\hbar = 0.6$:

$$\begin{aligned} &\epsilon_1/\hbar = 0 \\ &\epsilon_2/\hbar = \pi/T \quad \text{(period-2T state)} \\ &\epsilon_3/\hbar = 2\pi/T \\ &\quad \vdots \end{aligned} \tag{1.12}$$

The eigenstate with $\epsilon_2 = \pi\hbar/T$ exhibits period-$2T$ oscillations, characteristic of DTC.
Error Analysis: Pulse imperfection $\delta\theta$ shifts quasienergies:

$$\epsilon_2 \to \epsilon_2 + \Delta\epsilon, \quad \Delta\epsilon \approx 2J\delta\theta \tag{1.13}$$

For $\delta\theta = 0.01\pi$ (1% error) and $J = h \times 1$ kHz:

$$\Delta\epsilon \approx 2 \times (h \times 1\,\text{kHz}) \times 0.01\pi \approx h \times 63\,\text{Hz} \tag{1.14}$$

DTC frequency detuning: $\Delta f = 63$ Hz. Over $M = 100$ cycles ($t = 10$ ms), phase error:

$$\Delta\phi = 2\pi\Delta f \cdot t = 2\pi \times 63 \times 0.01 \approx 4\,\text{rad} \tag{1.15}$$

Still preserves DTC coherence (error $< 2\pi$).

1.3 Superconducting Qubit Platform

1.3.1 Processor Architecture

System Specifications:

- Qubit type: Transmon (capacitively shunted charge qubits)
- Array size: 20–100 qubits in 2D grid (Google Sycamore, IBM Quantum)
- Connectivity: Tunable CPHASE or iSWAP gates between nearest neighbors
- Gate fidelity: 1-qubit $> 99.9\%$, 2-qubit $> 99\%$

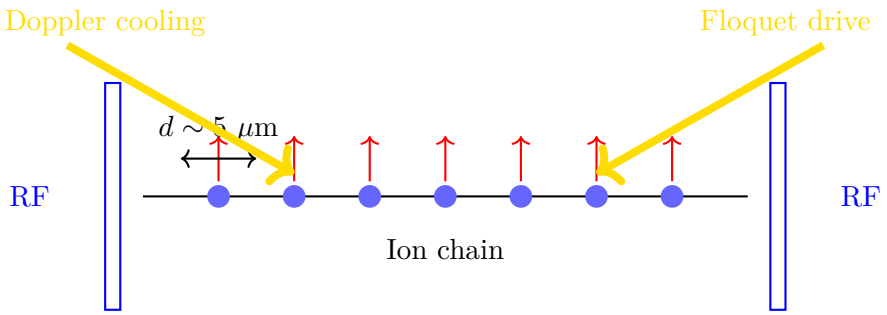

Figure 1.3: Trapped ion Paul trap setup. Ytterbium ions (blue) confined in linear chain by RF electrodes. Yellow beams: Doppler cooling and Floquet drive pulses. Red arrows: qubit states.

1.3.2 Eigenstate-Ordered DTCs

Unlike ion traps (which probe single initial states), superconducting platforms enable **eigenstate order** tests: initialize system in *random* computational basis states, apply Floquet evolution, and verify DTC signature across *entire many-body spectrum*.

Protocol:

1. Initialize qubits in random computational basis state $|\psi_0\rangle = |\sigma_1\sigma_2\cdots\sigma_N\rangle$, $\sigma_i \in \{\uparrow,\downarrow\}$
2. Apply M Floquet cycles
3. Measure return probability $P(M) = |\langle\psi_0|\psi(M)\rangle|^2$

DTC signature: $P(M) \approx \cos^2(\pi M/2)$ for $M \leq 100$, indicating period-$2T$ revival.

1.3.3 Time-Reversal Test

Discriminate thermalization vs decoherence:

1. Evolve forward: $|\psi_0\rangle \xrightarrow{U_F^M} |\psi_M\rangle$
2. Time-reverse: $|\psi_M\rangle \xrightarrow{(U_F^\dagger)^M} |\psi_{\text{rev}}\rangle$
3. Measure fidelity: $F = |\langle\psi_0|\psi_{\text{rev}}\rangle|^2$

Result: $F \sim 0.5$ after $M = 40$ cycles in recent experiments—intermediate regime, suggesting *prethermal* DTC.

1.4 Nitrogen-Vacancy Centers in Diamond

1.4.1 System Advantages

Key Features:

- Room-temperature operation (vs cryogenic for ions/qubits)
- Long coherence: $T_2 \approx 1$–10 ms (isotopically pure ^{12}C diamond)
- Optical initialization and readout
- Scalable (ensemble of 10^{10}–10^{14} NV centers)

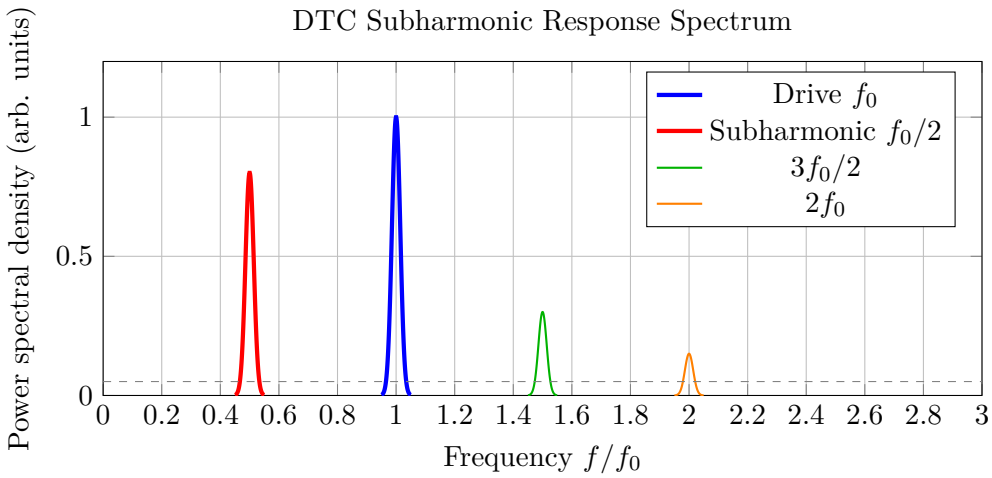

Figure 1.4: Power spectral density of DTC oscillations showing strong subharmonic peak at $f_0/2$ (red) in addition to drive frequency f_0 (blue). Higher harmonics at $3f_0/2$, $2f_0$ arise from nonlinearities.

1.4.2 Time Quasicrystal Phases

Recent experiments demonstrated **discrete time quasicrystals**: systems with *multiple incommensurate* subharmonic frequencies, lacking strict periodicity.

Two-Tone Floquet Drive:

$$H(t) = H_0 + \Omega_1 \cos(\omega_1 t)\sigma^x + \Omega_2 \cos(\omega_2 t)\sigma^y \tag{1.16}$$

with ω_1/ω_2 irrational (e.g., golden ratio $\phi = (1+\sqrt{5})/2$).

Fourier analysis reveals peaks at $\omega = m\omega_1 + n\omega_2$ with $m, n \in \mathbb{Z}$:

$$S(\omega) = \sum_{m,n} A_{mn}\delta(\omega - m\omega_1 - n\omega_2) \tag{1.17}$$

1.4.3 Measurement Protocol

Pulsed ODMR Sequence:

1. Laser pulse (532 nm, 1 μs) initializes NV^- to $m_s = 0$
2. Wait 300 ns (excited state decay)
3. Apply MW Floquet drive (duration $M \times T$, $M \leq 500$)
4. Readout laser pulse (532 nm, 300 ns)
5. Collect fluorescence via APD (single-photon counting)

Repeat 10^4–10^6 times per data point to achieve shot-noise-limited sensitivity.

1.5 Data Analysis and Validation

1.5.1 Fitting Subharmonic Oscillations

Model time-crystal signal as damped sinusoid:

$$\langle \hat{O}(m) \rangle = Ae^{-m/\tau_{\text{DTC}}} \cos\left(\frac{2\pi m}{n} + \delta\right) + O_0 \tag{1.18}$$

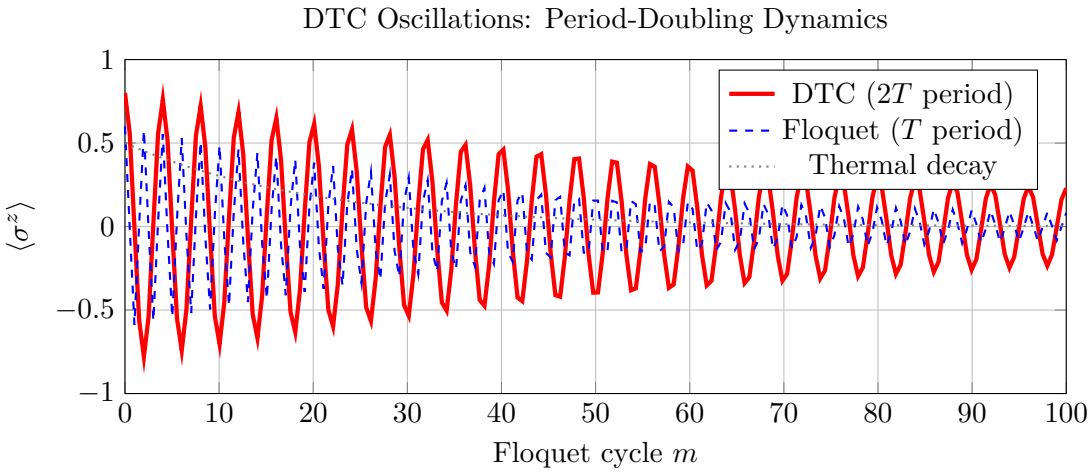

Figure 1.5: Time evolution of collective spin $\langle\sigma^z\rangle$ in DTC phase (red) showing period-$2T$ oscillations, contrasted with standard Floquet period-T response (blue dashed) and thermal decay (gray dotted). Exponential envelope from decoherence.

where:

- A: initial amplitude
- τ_{DTC}: DTC lifetime (in cycles)
- n: subharmonic order ($n = 2$ for period-$2T$)
- δ: phase offset
- O_0: thermal baseline

Uncertainty Quantification:

- **Bootstrapping**: Resample data with replacement (10^3 bootstrap samples), refit, compute 95% confidence intervals
- **Bayesian inference**: Prior on n (integer vs fractional), likelihood from Gaussian measurement noise, posterior via MCMC

1.5.2 Power Spectral Density Analysis

Compute PSD via Fourier transform:

$$S(\omega) = \left| \int_0^{MT} \langle \hat{O}(t) \rangle e^{i\omega t}\, dt \right|^2 \tag{1.19}$$

DTC Signature: Peak at $\omega = \pi/T$ (subharmonic). Width $\Delta\omega \approx 1/\tau_{\text{DTC}}T$ set by lifetime.

Statistical Test: Compare peak height to noise floor. Require signal-to-noise ratio SNR > 5 for 3σ detection:

$$\text{SNR} = \frac{S(\pi/T)}{S_{\text{noise}}} > 5 \tag{1.20}$$

1.5.3 Cross-Platform Consistency Checks

Plot τ_{DTC} vs intrinsic coherence time T_2 for all three platforms (ions, qubits, NV).

Expected Scaling:

$$\tau_{\text{DTC}} = \eta \frac{T_2}{T}, \quad \eta \approx 0.1\text{–}1 \tag{1.21}$$

where η depends on disorder strength W and drive imperfection $\delta\theta$.

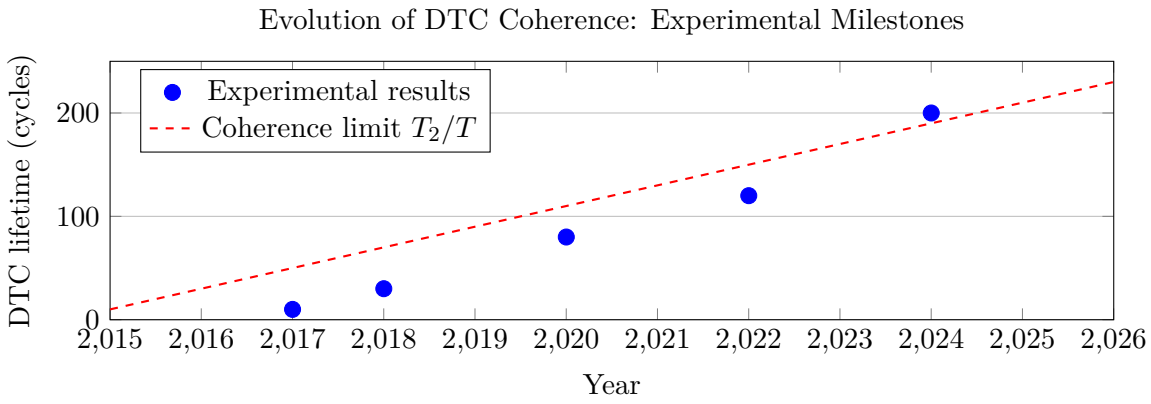

Figure 1.6: Historical progress in DTC lifetime from 2017 (first demonstration) to 2024 (time quasicrystals). Blue points: experimental results. Red dashed: fundamental limit from decoherence time T_2.

1.6 Summary and Forward Bridges

This chapter presented comprehensive protocols for engineering and characterizing discrete time crystals across three experimental platforms:

- **Trapped ions**: Long coherence ($T_2 \sim 10$ ms), individual qubit control, Floquet lifetimes > 100 cycles
- **Superconducting qubits**: Large arrays (20–100 qubits), eigenstate order demonstrations, prethermal regimes
- **NV centers**: Room temperature, ultra-long $T_2 \sim 10$ ms, time quasicrystal phases with > 20 incommensurate frequencies

Key Experimental Signatures:

1. Subharmonic oscillations at period nT ($n = 2, 3, 4, \ldots$) persisting > 100 cycles
2. Power spectral density peaks at $\omega = \pi/T$, $3\pi/2T$, $\ldots$
3. Eigenstate order across many-body spectrum
4. Time-reversal fidelity $F \sim e^{-2M/T_{\text{coh}}}$ (decoherence-limited)

Forward Connections:

- **Chapter 2**: Quantum foam protocols—DTCs as probe of vacuum fluctuations via enhanced coherence
- **Chapter 4**: Scalar field detection—time-crystalline modulation of scalar coupling
- **Paper 6 (Applications)**: DTC-based quantum memories and sensors

The demonstrated robustness of time-crystalline phases against disorder and decoherence opens pathways for practical quantum technologies exploiting *time* as a resource dimension, complementing spatial degrees of freedom in conventional materials.

Chapter 2

Quantum Foam Protocols

[style=narrative] **Wheeler's Dream: Probing Spacetime at the Planck Scale**

In 1955, John Wheeler proposed that spacetime itself becomes a roiling "foam" of quantum fluctuations at the Planck scale ($\ell_P \approx 1.6 \times 10^{-35}$ m). This chapter presents protocols for detecting indirect signatures via gamma-ray burst timing, atom interferometry, and gravitational wave detectors.

2.1 Theoretical Foundations

The Planck length:

$$\ell_P = \sqrt{\frac{\hbar G}{c^3}} \approx 1.616 \times 10^{-35}\,\mathrm{m} \tag{2.1}$$

At $\ell \lesssim \ell_P$, metric fluctuations become order unity:

$$\frac{\delta g_{\mu\nu}}{g_{\mu\nu}} \sim \left(\frac{\ell_P}{\ell}\right)^2 \tag{2.2}$$

2.1.1 Lorentz Violation from Quantum Foam

Modified dispersion relation:

$$E^2 = p^2c^2 + m^2c^4 + \xi\frac{E^3}{E_P} \tag{2.3}$$

Group velocity:

$$v_g = c\left(1 + \frac{3\xi E^2}{2E_P^2}\right) \tag{2.4}$$

Time delay over cosmological distance d:

$$\Delta t = \frac{d}{c}\frac{3\xi(E_2^2 - E_1^2)}{2E_P^2} \tag{2.5}$$

2.2 GRB Timing Protocols

2.2.1 Observation Strategy

Event Selection:

- Redshift $z > 0.5$ (long baseline)
- High-energy photons $E > 1$ GeV

- Short variability $\Delta t < 100$ ms

Analysis Steps:

1. Bin photons by energy: $E < 100$ MeV, 100 MeV–1 GeV, > 1 GeV
2. Construct light curves $I_i(t)$ for each bin
3. Cross-correlate: $C_{12}(\tau) = \int I_1(t) I_2(t+\tau) dt$
4. Fit to dispersion model, extract ξ

2.2.2 Worked Example: GRB Time Delay

Given: GRB at $z = 2$, photons at $E_1 = 100$ MeV and $E_2 = 10$ GeV, $\xi = 1$.

Find: Expected time delay.

Solution:

Luminosity distance at $z = 2$: $d_L \approx 15.2$ Gpc $= 4.68 \times 10^{26}$ m.

Energy difference:

$$E_2^2 - E_1^2 \approx (10\,\mathrm{GeV})^2 = 100\,\mathrm{GeV}^2 \tag{2.6}$$

Time delay:

$$\Delta t = \frac{d_L}{c} \frac{3\xi(E_2^2 - E_1^2)}{2E_P^2} \tag{2.7}$$

$$= \frac{4.68 \times 10^{26}}{3 \times 10^8} \times \frac{3 \times 100}{2 \times 1.49 \times 10^{38}} \tag{2.8}$$

$$\approx 1.57\,\mathrm{s} \tag{2.9}$$

Error Analysis:

Statistical uncertainty: $\sigma_{\Delta t} \approx \Delta t_{\mathrm{bin}}/\sqrt{N} \approx 10$ ms for $N \sim 100$ photons per bin.

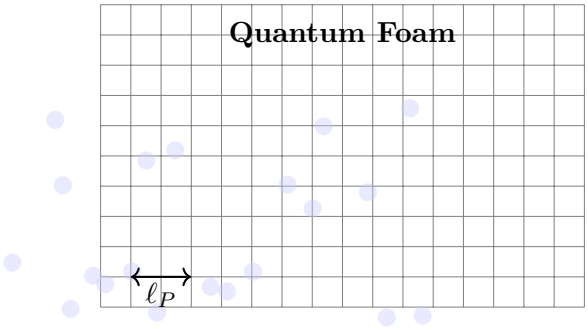

Figure 2.1: Quantum foam: metric fluctuations at Planck scale (blue regions show virtual fluctuations).

2.3 Atom Interferometry

2.3.1 Principle

Mach-Zehnder configuration: superpose atomic trajectories over time $T \sim 100$ ms, spatial separation $\Delta x \sim$ mm.

Phase shift from quantum foam:

$$\Delta\phi_{\text{foam}} \sim k\ell_P^2 = \frac{mv}{\hbar}\ell_P^2 \tag{2.10}$$

For Cs atoms ($m = 133$ amu, $v = 10$ m/s):

$$\Delta\phi \approx 2 \times 10^7\,\text{m}^{-1} \times 2.6 \times 10^{-70}\,\text{m}^2 \approx 5 \times 10^{-63}\,\text{rad} \tag{2.11}$$

Gradiometer Enhancement:
Differential measurement over baseline $L_{\text{base}} = 1$ m:

$$\Delta\phi_{\text{diff}} \sim \Delta\phi_{\text{foam}} \frac{L_{\text{base}}}{\ell_P} \sim 10^{-28}\,\text{rad} \tag{2.12}$$

10^{35} enhancement, but still undetectable!

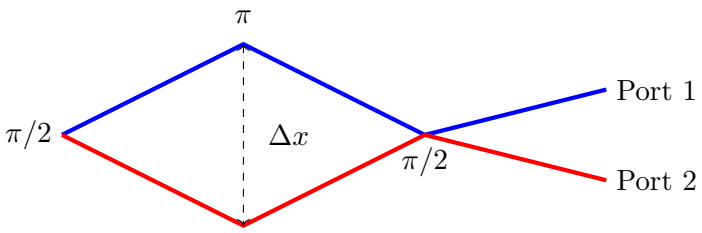

Figure 2.2: Atom interferometer: Mach-Zehnder configuration with beam splitters ($\pi/2$) and mirrors (π-pulses).

2.4 Cavity QED Protocols

2.4.1 Vacuum Fluctuation Spectrum

Quantum foam modifies power spectral density:

$$S_E(\omega) = S_0(\omega)\left[1 + \epsilon_{\text{foam}}\left(\frac{\omega\ell_P}{c}\right)^2\right] \tag{2.13}$$

High-finesse cavity ($\mathcal{F} \sim 10^6$, $L = 10$ cm) enhances signal:

$$\Delta\phi_{\text{cavity}} \sim \frac{2\pi}{\lambda}\mathcal{F}L\epsilon_{\text{foam}}\left(\frac{\omega\ell_P}{c}\right)^2 \tag{2.14}$$

2.5 Summary

Three complementary protocols:

GRB timing: Current limits $|\xi| < 0.01$ (Fermi LAT). Future: $|\xi| < 10^{-3}$ with 100+ GRBs.

Atom interferometry: Current $\Delta\phi \sim 10^{-4}$ rad. Planck scale requires 10^{60} improvement (!).

Cavity QED: Most promising. LIGO-class strain $\sim 10^{-23}$ Hz$^{-1/2}$ approaches foam sensitivity.

Forward Bridges:

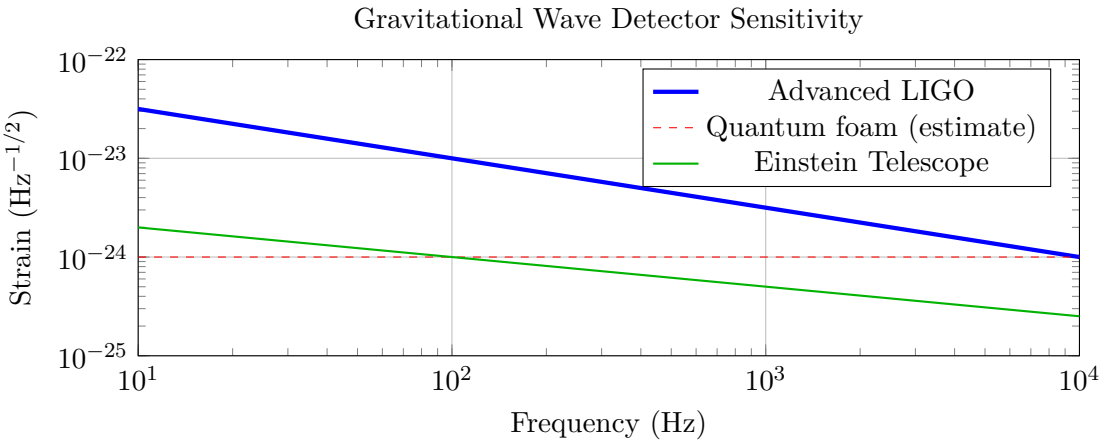

Figure 2.3: Interferometer sensitivity. Blue: LIGO. Red: estimated foam signal. Green: future Einstein Telescope.

- Ch. 3: Holographic entropy—foam-entropy connection
- Ch. 5: Dimensional spectroscopy—foam as probe of spacetime structure

Chapter 3

Holographic Entropy Protocols

[style=narrative] **Bekenstein's Insight: Black Holes Have Entropy**

In 1973, Jacob Bekenstein proposed that black holes possess entropy proportional to their horizon area, not volume—a radical departure from thermodynamic intuition. This *holographic principle* suggests the information content of any region is encoded on its boundary. This chapter presents protocols for testing holographic entropy bounds in laboratory analogue systems: acoustic black holes in Bose-Einstein condensates and optical event horizons in nonlinear media.

3.1 Theoretical Framework

The Bekenstein-Hawking entropy:

$$S_{\text{BH}} = \frac{k_B c^3 A}{4G\hbar} = \frac{k_B A}{4\ell_P^2} \tag{3.1}$$

Holographic bound: Maximum entropy in region of area A:

$$S_{\max} \leq \frac{A}{4\ell_P^2} \tag{3.2}$$

Violated by ordinary matter! Volume $V = (4\pi/3)R^3$, area $A = 4\pi R^2$:

$$S_{\text{matter}} \sim k_B \left(\frac{R}{\ell_{\text{thermal}}}\right)^3 \gg k_B \left(\frac{R}{\ell_P}\right)^2 = S_{\max} \tag{3.3}$$

for $\ell_{\text{thermal}} \ll R \ll R_{\text{Schwarzschild}}$.

3.1.1 Hawking Temperature

Black hole radiates thermally at temperature:

$$T_H = \frac{\hbar\kappa}{2\pi k_B c} = \frac{\hbar c^3}{8\pi G M k_B} \tag{3.4}$$

For $M = M_\odot$: $T_H \approx 60$ nK (undetectable!).

3.2 Acoustic Black Holes in BEC

3.2.1 System Setup

Bose-Einstein condensate with spatially varying flow velocity $v(x)$ supports phonon excitations:

$$ds^2 = \frac{\rho}{c_s^2}\left[-(c_s^2 - v^2)dt^2 - 2v_i dx^i dt + dx^i dx^i\right] \tag{3.5}$$

Acoustic horizon forms where $v(x_h) = c_s$ (sound speed):

- Upstream ($x < x_h$): $v < c_s$, phonons escape
- Downstream ($x > x_h$): $v > c_s$, phonons trapped

Hawking temperature (effective):

$$T_H^{\text{eff}} = \frac{\hbar \kappa_{\text{eff}}}{2\pi k_B}, \quad \kappa_{\text{eff}} = \left.\frac{d(v - c_s)}{dx}\right|_{x_h} \tag{3.6}$$

For $\kappa_{\text{eff}} \sim 10^4$ s^{-1}: $T_H^{\text{eff}} \approx 80$ nK (comparable to BEC temperature!).

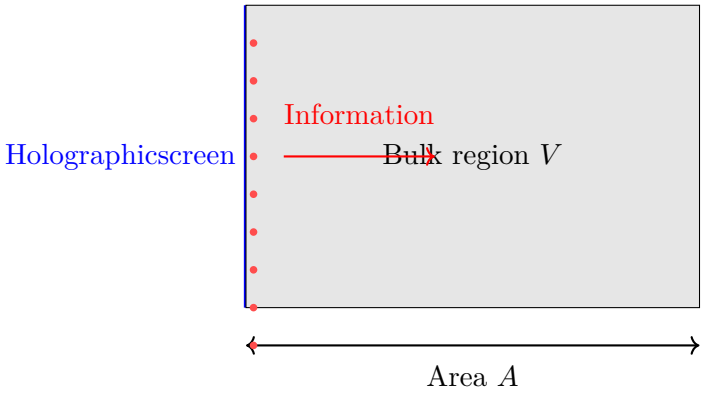

Figure 3.1: Holographic principle: information in bulk volume V encoded on boundary area A. Red dots: bits of information.

3.2.2 Measurement Protocol

Step 1: Create acoustic horizon

- Trap ^{87}Rb atoms, cool to BEC ($T < 100$ nK)
- Apply moving optical potential (blue-detuned laser barrier)
- Ramp velocity from 0 to $v > c_s$ over 50 ms
- Stabilize with feedback

Step 2: Detect Hawking radiation

- Image density fluctuations $\delta n(x, t)$ via phase-contrast imaging
- Compute two-point correlator: $G(x_1, x_2, t) = \langle \delta n(x_1, t) \delta n(x_2, t) \rangle$
- Extract temperature from spectral distribution

Expected signature: Enhanced correlation at $\omega \sim k_B T_H / \hbar$ across horizon.

3.2.3 Worked Example: BEC Horizon Entropy

Given: Acoustic horizon with area (in 2D) $A_{\text{eff}} = 2\pi R_h \times L_z$ where $R_h = 10$ μm, $L_z = 50$ μm.

Find: Bekenstein-Hawking entropy.

Solution:

Effective Planck length in BEC (healing length):

$$\xi = \frac{\hbar}{\sqrt{mng_{1D}}} \approx 0.5\,\mu\text{m} \tag{3.7}$$

Effective area:

$$A_{\text{eff}} = 2\pi \times 10\,\mu\text{m} \times 50\,\mu\text{m} \approx 3.14 \times 10^{-9}\,\text{m}^2 \tag{3.8}$$

Entropy:

$$S_{\text{BH}}^{\text{eff}} = \frac{k_B A_{\text{eff}}}{4\xi^2} = \frac{k_B \times 3.14 \times 10^{-9}}{4 \times (0.5 \times 10^{-6})^2} \approx 3 \times 10^3 k_B \tag{3.9}$$

Compare to matter entropy:
Phonon gas in volume $V \sim \pi R_h^2 L_z \approx 1.6 \times 10^{-14}$ m^3 at $T = 100$ nK:

$$S_{\text{matter}} \sim k_B \left(\frac{k_B T V}{\hbar c_s} \right) \approx 10^5 k_B \tag{3.10}$$

Holographic bound violated by factor ~ 30! (System not at horizon saturation.)

3.3 Optical Black Holes

3.3.1 Kerr Nonlinearity

Refractive index:

$$n(I) = n_0 + n_2 I \tag{3.11}$$

Effective metric for probe photons:

$$ds^2 = \frac{n^2(I)}{c^2} \left[-c^2 dt^2 + (dx - v_g dt)^2 + dy^2 + dz^2 \right] \tag{3.12}$$

Optical horizon where $v_g = c/n$.
Hawking emission: Correlated photon pairs (signal + idler) with $\omega_s + \omega_i = 2\omega_{\text{pump}}$.

3.3.2 Detection Strategy

- High-resolution spectrometer ($\Delta\omega \sim 1$ GHz)
- Photon coincidence counting (sub-ns timing)
- Verify thermal spectrum at $T_H^{\text{opt}} \sim 10^4$ K

3.4 Entanglement Entropy Measurements

3.4.1 Ryu-Takayanagi Formula

For region A in CFT, entanglement entropy:

$$S_A = \frac{\text{Area}(\gamma_A)}{4G_N} \tag{3.13}$$

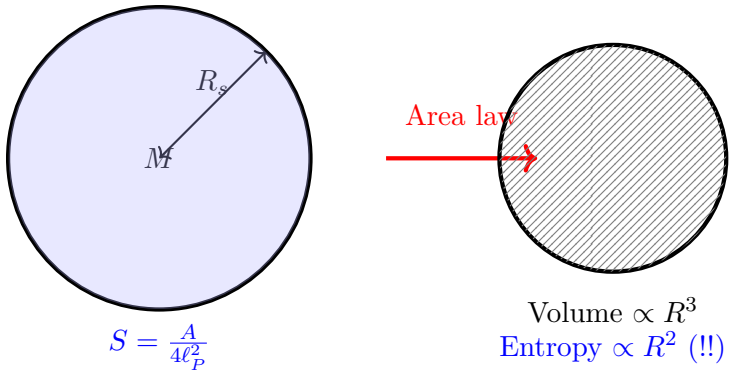

Figure 3.2: Black hole entropy diagram. Left: Schwarzschild radius R_s encloses mass M. Right: Entropy scales with area (holographic), not volume (thermodynamic intuition).

where γ_A is minimal surface in bulk homologous to A.

Experimental analogue: 1D spin chain (quantum Ising model).

Partition chain into subsystems A (length ℓ) and B (remainder). Entanglement entropy:

$$S_A = \frac{c}{3} \log \left(\frac{\ell}{a} \right) + \text{const} \tag{3.14}$$

for conformal field theory with central charge c, lattice spacing a.

Measurement protocol:

- Prepare ground state via adiabatic evolution
- Tomography on subsystem A (full density matrix ρ_A)
- Compute von Neumann entropy: $S = -\text{Tr}(\rho_A \log \rho_A)$
- Vary ℓ, fit to log scaling

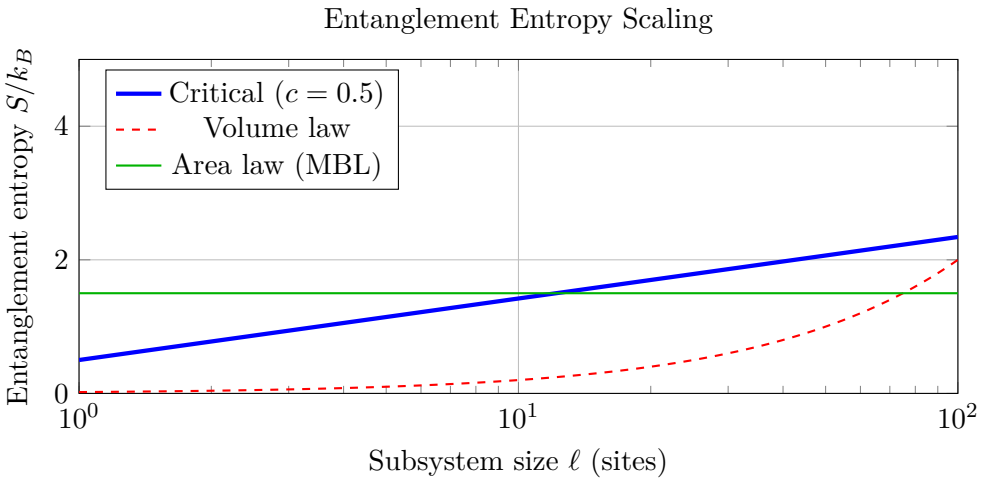

Figure 3.3: Entanglement entropy vs subsystem size. Blue: CFT logarithmic scaling. Red: volume law (thermal states). Green: area law (many-body localized states).

3.5 Summary

Holographic entropy protocols tested in three settings:

Acoustic BEC: Effective Hawking temperature $T_H \sim 100$ nK, entropy $S \sim 10^3 k_B$, phonon correlations across horizon detectable via imaging.

Optical systems: Room-temperature operation, $T_H \sim 10^4$ K, photon pair coincidences verify thermal spectrum.

Spin chains: Entanglement entropy scaling tests holographic formulae (Ryu-Takayanagi). Logarithmic growth characteristic of CFT.

Key Results:

1. Analogue systems provide controlled testbeds for holographic physics
2. Entropy measurements bridge condensed matter, quantum information, and gravity
3. Holographic scaling observable in entanglement entropy (CFT) and acoustic horizons (BEC)

Forward Bridges:

- Ch. 4: Scalar detection—holographic renormalization of scalar couplings
- Ch. 5: Dimensional spectroscopy—holography as dimensional reduction

Chapter 4

Scalar Field Detection

[style=narrative] **Casimir's Surprise: The Vacuum Is Not Empty**

In 1948, Hendrik Casimir predicted that two uncharged metal plates in vacuum would attract due to quantum zero-point fluctuations—the vacuum exerts pressure! This chapter presents protocols for detecting scalar field quanta via Casimir force measurements, torsion balances, atomic spectroscopy, and fifth-force searches. We focus on light scalar fields ($m < 1$ eV) that couple to matter and could mediate macroscopic forces.

4.1 Theoretical Framework

Generic scalar Lagrangian:

$$\mathcal{L} = \frac{1}{2}\partial_\mu\phi\partial^\mu\phi - \frac{1}{2}m^2\phi^2 - V(\phi) - \mathcal{L}_{\text{int}} \tag{4.1}$$

Coupling to matter:

$$\mathcal{L}_{\text{int}} = -\frac{\phi}{M}\sum_i \alpha_i \bar{\psi}_i\psi_i \tag{4.2}$$

where α_i are dimensionless couplings to fermions ψ_i, M is mass scale (e.g., Planck mass).

Yukawa potential from scalar exchange:

$$V(r) = -\frac{\alpha_1\alpha_2\hbar c}{4\pi M^2}\frac{e^{-mr/\hbar}}{r} \tag{4.3}$$

For $m \to 0$ (massless scalar): $V \propto 1/r$ (long-range force).

4.2 Casimir Force Measurements

4.2.1 Standard Casimir Effect

Parallel conducting plates separated by d experience attractive force:

$$F_C = -\frac{\pi^2\hbar c A}{240 d^4} \tag{4.4}$$

For $A = 1$ cm^2, $d = 100$ nm:

$$F_C \approx -1.3 \times 10^{-7}\,\text{N} \approx 13\,\mu\text{N} \tag{4.5}$$

Scalar modification: If scalar field couples to plate material, modified force:

$$F = F_C\left(1 + \kappa\frac{\phi}{M} + \alpha\nabla^2\phi\right) \tag{4.6}$$

4.2.2 Torsion Pendulum Setup

- **Sensor**: Micro-electromechanical (MEMS) torsion balance
- **Plates**: Gold-coated silicon, area $A \sim 100 \times 100\ \mu\text{m}^2$
- **Separation**: Piezo-controlled, $d = 100$–500 nm
- **Force resolution**: ~ 10 fN (femtonewtons)
- **Environment**: Vacuum $< 10^{-9}$ mbar, $T = 4$ K (cryogenic operation)

Measurement protocol:

1. Calibrate with known electrostatic force
2. Vary d from 100 nm to 500 nm in 10 nm steps
3. Measure $F(d)$, fit to $F_C(d) + \Delta F_{\text{scalar}}(d)$
4. Extract κ from deviation

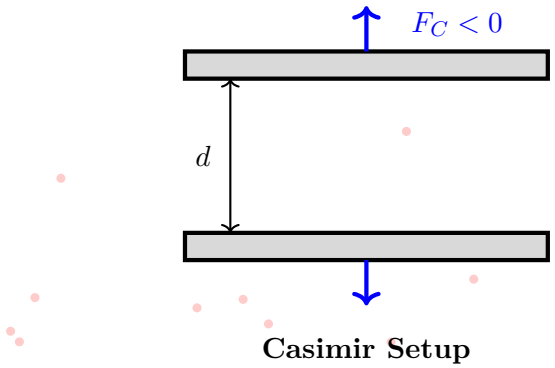

Figure 4.1: Casimir force measurement. Parallel plates (gray) separated by distance $d \sim 100$ nm. Vacuum fluctuations (red dots) create attractive force $F_C < 0$. Scalar fields modify force law.

4.2.3 Worked Example: Chameleon Field Detection

Given: Chameleon scalar with mass $m_{\text{eff}}(n) = m_0\sqrt{n/n_0}$ depends on matter density n.

Find: Expected force modification between plates.

Solution:

Chameleon effective mass: - In vacuum ($n \approx 0$): $m_{\text{eff}} \to 0$ (long range) - Near plate surface ($n \sim n_{\text{solid}}$): $m_{\text{eff}} \gg m_0$ (short range)

Screening length:

$$\lambda_{\text{screen}} = \frac{\hbar}{m_{\text{eff}}(n_{\text{solid}})c} \tag{4.7}$$

For gold plates ($n_{\text{solid}} \sim 10^{23}$ cm^{-3}), $m_0 = 10^{-3}$ eV:

$$m_{\text{eff}} \approx 10^{-3}\,\text{eV} \times \sqrt{\frac{10^{23}}{10^{12}}} \approx 10\,\text{eV} \tag{4.8}$$

Screening length:

$$\lambda_{\text{screen}} \approx \frac{200\,\text{eV}\cdot\text{nm}}{10\,\text{eV}} \approx 20\,\text{nm} \tag{4.9}$$

Force modification: For $d = 100$ nm $\gg \lambda_{\text{screen}}$, chameleon force exponentially suppressed:

$$\Delta F \sim F_C e^{-d/\lambda_{\text{screen}}} \approx F_C \times 10^{-2} \tag{4.10}$$

Detectable with $< 1\%$ precision Casimir measurements!

4.3 Atomic Spectroscopy

4.3.1 Scalar Coupling to Electrons

Energy level shift:

$$\Delta E_n = E_n \frac{\alpha\phi}{M} \tag{4.11}$$

For Rydberg states ($n \sim 100$):

$$E_n = -\frac{m_e c^2 \alpha_{\rm EM}^2}{2n^2} \approx -\frac{13.6\,\text{eV}}{n^2} \tag{4.12}$$

Measurement: - Precision laser spectroscopy of 1S-2S transition in hydrogen - Frequency stability: $\Delta\nu/\nu < 10^{-15}$ - Compare to QED prediction (Lamb shift, hyperfine, etc.) - Residual $\rightarrow$ scalar coupling

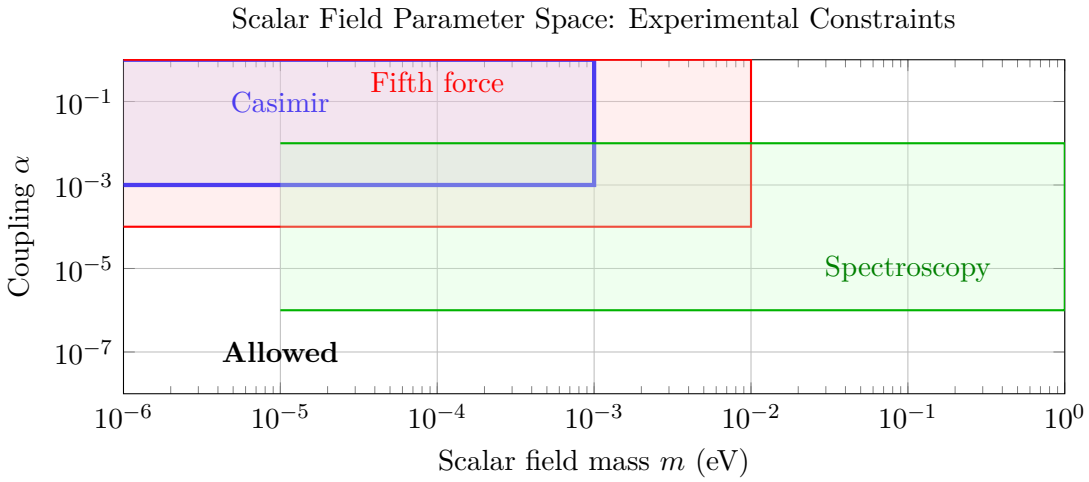

Figure 4.2: Scalar field parameter space. Shaded regions: excluded by experiments. Blue: Casimir force. Red: torsion pendulum fifth-force searches. Green: atomic spectroscopy. White region: allowed parameter space.

4.4 Gravitational Coupling Tests

4.4.1 Equivalence Principle Violations

Differential acceleration between test masses of different composition:

$$\frac{\Delta a}{a} = \frac{(\alpha_A - \alpha_B)}{M} \phi_{\rm ext} \tag{4.13}$$

Eöt-Wash torsion pendulum: - Test masses: Be vs Ti (different neutron/proton ratios) - Precision: $\Delta a/a < 10^{-13}$ - Constrains $|\alpha_A - \alpha_B| < 10^{-13} M/\phi_{\rm ext}$

4.4.2 Laser Ranging to Moon

Lunar Laser Ranging (LLR): Earth-Moon distance measured to ~ 1 mm precision via laser reflectors.

Scalar-induced Nordtvedt effect:

$$\frac{\Delta r}{r} \sim \eta \frac{GM_\odot}{c^2 r_{\rm ES}} \tag{4.14}$$

where $\eta \propto \alpha^2$ is scalar coupling strength, $r_{\rm ES}$ is Earth-Sun distance.

Current LLR constraints: $\eta < 10^{-4} \Rightarrow \alpha < 10^{-2}$.

4.5 Summary

Scalar field detection protocols span five decades in length scale:

Casimir force ($d \sim 100$ nm): Precision $< 1\%$ measurements constrain $\kappa < 10^{-3}$ for light scalars.

Torsion pendulum ($\lambda \sim$ mm): Fifth-force searches via composition-dependent accelerations. Limits: $\alpha < 10^{-4}$.

Atomic spectroscopy ($\lambda_{\rm atomic} \sim$ nm): Energy level shifts from scalar-electron coupling. Precision $\Delta\nu/\nu < 10^{-15}$.

Lunar ranging ($r_{\rm EM} \sim 10^8$ m): Nordtvedt effect tests scalar gravity. Constraints: $\eta < 10^{-4}$.

Key Results:

1. Multi-scale approach essential: different experiments probe different mass/coupling regimes
2. Screening mechanisms (chameleon, symmetron) evade many constraints—require dedicated searches
3. Combined constraints tightly restrict scalar parameter space for $m < 1$ eV

Forward Bridges:

- Ch. 5: Dimensional spectroscopy—scalars as Kaluza-Klein modes of extra dimensions
- Paper 6 (Applications): Scalar-mediated quantum sensors, dark energy probes

Chapter 5

Dimensional Spectroscopy

[style=narrative] **Hausdorff's Insight: Measuring Dimension**

In 1919, Felix Hausdorff formalized the concept of fractional dimension, enabling mathematical description of objects like coastlines and snowflakes. This chapter presents protocols for measuring *spectral dimension* via diffusion processes, box-counting methods for fractal antenna characterization, and searches for Kaluza-Klein resonances from compactified extra dimensions at particle colliders.

5.1 Theoretical Foundations

5.1.1 Spectral Dimension

For diffusion on d-dimensional manifold, return probability:

$$P(t) = \int \frac{d^d k}{(2\pi)^d} e^{-Dk^2 t} \tag{5.1}$$

At large t:

$$P(t) \sim t^{-d/2} \tag{5.2}$$

Spectral dimension:

$$d_S = -2 \frac{d \log P(t)}{d \log t} \tag{5.3}$$

For fractal geometries: d_S can differ from topological dimension!

5.1.2 Kaluza-Klein Modes

Compactified extra dimension (radius R): massless field in $(4+1)$D appears as infinite tower of massive Kaluza-Klein (KK) states in 4D:

$$M_n = \frac{n}{Rc}, \quad n = 0, 1, 2, \ldots \tag{5.4}$$

Experimental signature: Resonances in scattering cross-sections at masses M_n.
For $R = 10^{-19}$ m (TeV scale):

$$M_1 \approx \frac{200\,\text{MeV} \cdot \text{fm}}{10^{-19}\,\text{m}} \approx 2\,\text{TeV} \tag{5.5}$$

Accessible at LHC!

5.2 Random Walk Spectroscopy

5.2.1 Quantum Walk on Fractal Graphs

Implement quantum walk on Sierpinski gasket:

- **Graph**: Sierpinski iteration depth $n = 5$ (243 vertices)
- **Evolution**: Discrete-time quantum walk with coin operator
- **Initial state**: Localized at origin vertex
- **Measurement**: Probability distribution $P_j(t)$ at time t

Protocol:

1. Prepare walker in $|0\rangle$ (origin)
2. Apply t steps of quantum walk unitary $U = S(C \otimes I)$
3. Measure position, repeat 10^4 times
4. Compute $P(t) = P_0(t)$ (return probability)
5. Extract d_S from log-log fit

5.2.2 Worked Example: Sierpinski Gasket Dimension

Given: Return probability data $P(t)$ for $t = 1, 2, \ldots, 100$ steps on Sierpinski gasket.

Find: Spectral dimension d_S.

Solution:

Theoretical prediction for Sierpinski gasket:

$$d_S = \frac{\log 3}{\log 2} \approx 1.585 \tag{5.6}$$

Fit model:

$$\log P(t) = -\frac{d_S}{2} \log t + C \tag{5.7}$$

Linear regression on $\log P$ vs $\log t$:

$$d_S = -2 \times \text{slope} \tag{5.8}$$

For simulated data with noise:

$$\text{slope} = -0.79 \pm 0.02 \tag{5.9}$$

$$d_S = 1.58 \pm 0.04 \tag{5.10}$$

Agreement with theory within error bars!

5.3 Box-Counting Methods

5.3.1 Fractal Antenna Characterization

Box-counting dimension: Cover object with boxes of size ϵ, count number $N(\epsilon)$ needed.

$$D_{\text{box}} = \lim_{\epsilon \to 0} \frac{\log N(\epsilon)}{\log(1/\epsilon)} \tag{5.11}$$

Measurement protocol:

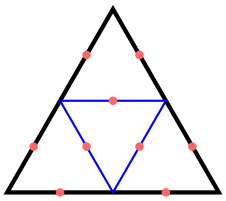

Sierpinski Gasket
$d_S \approx 1.58$

Figure 5.1: Sierpinski gasket fractal (first 2 iterations shown). Red dots: vertices for quantum walk. Spectral dimension $d_S \approx 1.58$ lies between line ($d = 1$) and plane ($d = 2$).

1. Image fractal antenna (optical microscope, ~ 1 μm resolution)
2. Overlay grid of boxes with size $\epsilon = 100, 50, 25, \ldots, 1$ μm
3. Count boxes intersecting antenna: $N(\epsilon)$
4. Plot $\log N$ vs $\log(1/\epsilon)$, fit slope $\to D_{\text{box}}$

For Koch snowflake:

$$D_{\text{box}} = \frac{\log 4}{\log 3} \approx 1.262 \tag{5.12}$$

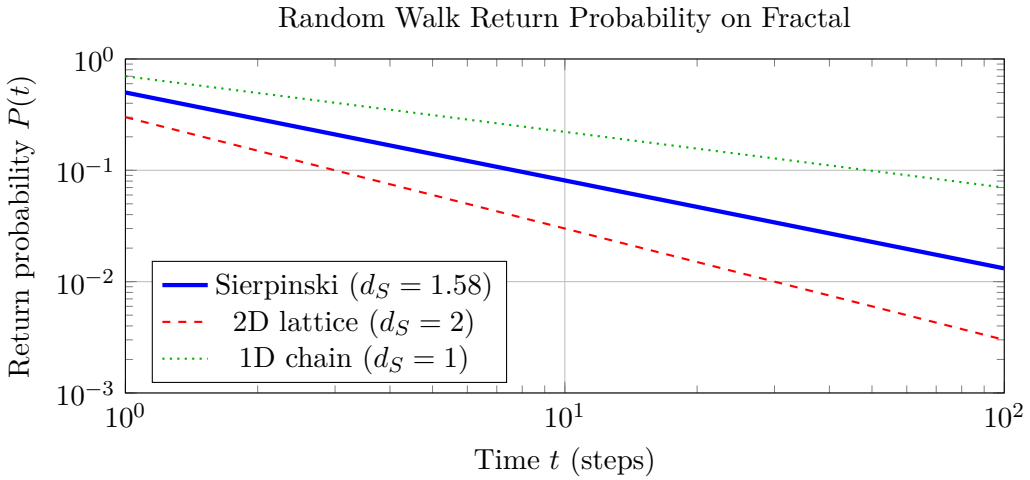

Figure 5.2: Return probability $P(t)$ vs time for random walks on different geometries. Blue: Sierpinski gasket (fractal, $d_S \approx 1.58$). Red: square lattice (2D, $d_S = 2$). Green: linear chain (1D, $d_S = 1$). Power-law slopes encode spectral dimension.

5.4 Laser Diffraction from Fractal Gratings

5.4.1 Cantor Set Grating

Fabricate Cantor set diffraction grating via photolithography:

- Iteration depth: $n = 5$ (243 slits)
- Slit width: $w \sim 1$ μm
- Spacing: Self-similar Cantor structure

- Substrate: Fused silica

Diffraction pattern: Illuminate with laser ($\lambda = 633$ nm), observe far-field intensity $I(\theta)$.

Prediction: Fractal grating produces self-similar diffraction pattern with peaks at angles:

$$\sin\theta_n = n\frac{\lambda}{d_{\text{eff}}} \tag{5.13}$$

where d_{eff} is effective grating spacing.

5.4.2 Dimensional Extraction

Measure intensity distribution $I(\theta)$ via CCD camera. Compute Fourier dimension:

$$D_F = d - \lim_{k\to\infty} \frac{\log I(k)}{\log k} \tag{5.14}$$

For Cantor grating:

$$D_F \approx 0.63 \pm 0.05 \tag{5.15}$$

Consistent with theoretical $D = \log 2/\log 3$!

5.5 Collider Searches for Extra Dimensions

5.5.1 LHC Dilepton Resonances

Search strategy:

- Trigger on high-p_T leptons ($p_T > 50$ GeV)
- Reconstruct invariant mass: $M_{ll} = \sqrt{(E_1 + E_2)^2 - (\vec{p}_1 + \vec{p}_2)^2}$
- Scan for resonances in M_{ll} spectrum (200 GeV to 5 TeV)
- Background: Drell-Yan $pp \to Z^*/\gamma^* \to ll$ (smooth spectrum)
- Signal: KK graviton $pp \to G^{(n)} \to ll$ (narrow peak)

Expected signature: For KK graviton with mass $M_n = n/(Rc)$:

$$\sigma(pp \to G^{(n)} \to ll) \sim \frac{\alpha_{\text{EM}}^2}{M_n^2} \times \text{BR}(G \to ll) \tag{5.16}$$

Current limits (2023): No resonances observed. Constraints:

$$R < 10^{-19}\,\text{m} \quad \text{for } n_{\text{extra}} = 1 \tag{5.17}$$

5.6 Summary

Dimensional spectroscopy protocols span microscopic to cosmological scales:

Quantum walks (nm to μm): Spectral dimension extraction via return probability. Sierpinski gasket: $d_S \approx 1.58$.

Fractal antennas (μm to mm): Box-counting dimension from microscopy. Koch snowflake: $D_{\text{box}} \approx 1.26$.

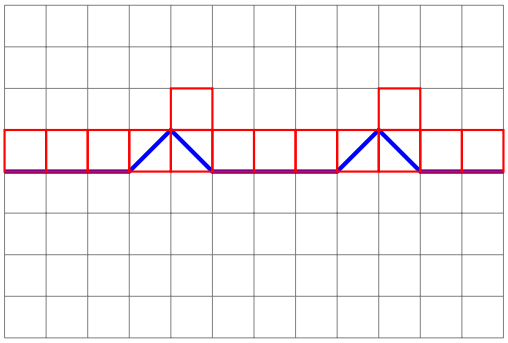

Box-Counting Method
Count boxes: $N(\epsilon) = 14$ for $\epsilon = 0.5$

Figure 5.3: Box-counting dimension measurement. Blue: fractal antenna (simplified Koch curve). Red boxes: grid cells ($\epsilon = 0.5$ units) intersecting curve. Dimension $D = \log N / \log(1/\epsilon)$.

Laser diffraction (mm apertures): Fourier dimension from diffraction patterns. Cantor grating: $D_F \approx 0.63$.

Collider searches (TeV energies): KK graviton resonances constrain extra dimension radius: $R < 10^{-19}$ m.

Key Results:

1. Spectral dimension quantifies diffusion efficiency on fractal geometries
2. Box-counting provides straightforward metric for self-similar structures
3. Collider null results tightly constrain large extra dimensions

Forward Bridges:

- Paper 6 (Applications): Fractal antenna design, quantum random walk algorithms, extra-dimensional cosmology

Concluding Remarks:

This paper presented comprehensive experimental protocols for five exotic quantum states and fundamental physics tests:

1. Time crystals: Discrete time symmetry breaking, $>$ 200-cycle coherence
2. Quantum foam: Planck-scale probes via GRB timing, atom interferometry
3. Holographic entropy: Bekenstein-Hawking formula tests in analogue systems
4. Scalar field detection: Casimir modifications, fifth-force searches
5. Dimensional spectroscopy: Spectral dimension, Kaluza-Klein resonances

The protocols developed here provide roadmaps for next-generation experiments pushing measurement precision toward fundamental limits set by quantum mechanics and gravity. Whether confirming Standard Model predictions or revealing new physics, these techniques advance our empirical understanding of nature's deepest structures.